

Design of electrocaloric materials based on *E-T* phase diagrams

Fei Han(韩飞), Rongju Zhong(钟容菊), Jikun Yang(杨继昆), Chuanbao Liu(刘传宝), and Yang Bai(白洋)
Citation: Chin. Phys. B, 2026, 35 (**2**): 027704. DOI: 10.1088/1674-1056/ae3308
http://cpb.iphy.ac.cn; http://iopscience.iop.org/cpb

What follows is a list of articles you may be interested in

Understanding thermal hysteresis of ferroelectric phase transitions in $BaTiO_3$ with combined first-principle-based approach and phase-field model

Cancan Shao(邵灿灿) and Houbing Huang(黄厚兵)
Chin. Phys. B, 2025, 34 (**2**): 027701. DOI: 10.1088/1674-1056/ad9e94

$BaTiO_3$/p-GaN/Au self-driven UV photodetector with bipolar photocurrent controlled by ferroelectric polarization

Wushuang Han(韩无双), Kewei Liu(刘可为), Jialin Yang(杨佳霖), Yongxue Zhu(朱勇学), Zhen Cheng(程祯), Xing Chen(陈星), Binghui Li(李炳辉), Lei Liu(刘雷), and Dezhen Shen(申德振)
Chin. Phys. B, 2024, 33 (**4**): 047701. DOI: 10.1088/1674-1056/ad2607

Tensile stress regulated microstructures and ferroelectric properties of $Hf_{0.5}Zr_{0.5}O_2$ films

Siying Huo(霍思颖), Junfeng Zheng(郑俊锋), Yuanyang Liu(刘远洋), Yushan Li(李育姗),Ruiqiang Tao(陶瑞强), Xubing Lu(陆旭兵), and Junming Liu(刘俊明)
Chin. Phys. B, 2023, 32 (**12**): 127701. DOI: 10.1088/1674-1056/acfb79

Structure instability-induced high dielectric properties in[001]-oriented $0.68Pb(Mg_{1/3}Nb_{2/3})O_3$-$0.33PbTiO_3$ crystals

Xiao-Juan Li(李晓娟), Xing Fan(樊星), Zeng-Zhe Xi(惠增哲), Peng Liu(刘鹏), Wei Long(龙伟), Pin-Yang Fang(方频阳), Rui-Hua Nan(南瑞华)
Chin. Phys. B, 2019, 28 (**5**): 057701. DOI: 10.1088/1674-1056/28/5/057701

Effect of an electric field on the electrocaloric response of ferroelectrics

Hongbo Liu(刘宏波)
Chin. Phys. B, 2018, 27 (**12**): 127701. DOI: 10.1088/1674-1056/27/12/127701

TOPICAL REVIEW — Multiferroicity and multicaloric effects

Design of electrocaloric materials based on E–T phase diagrams

Fei Han(韩飞)[1], Rongju Zhong(钟容菊)[1], Jikun Yang(杨继昆)[2], Chuanbao Liu(刘传宝)[1], and Yang Bai(白洋)[1,†]

[1] *Beijing Key Laboratory of Materials Intelligent Technology, Institute for Advanced Materials and Technology, University of Science and Technology Beijing, Beijing* 100083, *China*

[2] *Department of Physics, School of Mathematics and Physics, University of Science and Technology Beijing, Beijing* 100083, *China*

(Received 22 November 2025; revised manuscript received 27 December 2025; accepted manuscript online 4 January 2026)

As electronic technology continues to evolve towards miniaturization and integration, the demand for micro-refrigeration technology in microelectronic systems is increasing. Ferroelectric (FE) refrigeration technology based on the electrocaloric effect (ECE) has emerged as a highly promising candidate in this field, due to its advantages of high energy efficiency, simple structure, easy miniaturization, low cost, and environmental friendliness. The EC performance of FE materials essentially depends on the phase transition features under the coupled electric and thermal fields, making the E–T phase diagram a core tool for decoding the underlying mechanism of ECE. This paper reviews the development of EC materials, focusing on the comprehensive study of E–T phase diagrams. By correlating the microscopic phase structure of FE materials with the macroscopic physical properties, it clarifies the manipulation mechanism for enhanced ECE performance, providing theoretical support for the targeted design of high-performance EC materials. In the future, the introduction of data-driven methods is expected to enable the high-throughput construction of FE phase diagrams, thereby accelerating the optimization of high-performance EC materials and promoting the practical application of FE refrigeration technology.

Keywords: ferroelectric material, electrocaloric effect, phase diagram, phase transition, sold-state refrigeration

PACS: 77.80.–e, 77.80.bn, 77.84.–s

DOI: 10.1088/1674-1056/ae3308 **CSTR:** 32038.14.CPB.ae3308

1. Introduction

The rapid development of electronic technology toward miniaturization and integration has made micro-refrigeration technology an increasingly indispensable component of electronic systems. FE refrigeration technology based on the ECE offers high energy efficiency, simple device structure, easy miniaturization, convenient operation, low cost and environmental friendliness,[1–4] making it a highly promising solid-state refrigeration technology for microelectronics applications. In the past decade, the research on the ECE has developed rapidly, emerging as a brand-new hot direction in the field of ferroelectric research.

The ECE is a fundamental physical phenomenon in FE dipole systems, in which change in the external electric field induces reversible isothermal entropy change (ΔS) and/or adiabatic temperature change (ΔT) in the EC materials. Under normal circumstances, FE materials exhibit a positive ECE: under adiabatic conditions, applying an electric field aligns the disordered electric dipoles into an ordered state (entropy decreases), leading to a temperature increase ($\Delta T > 0$). Removing the electric field allows the dipoles to revert to a disordered state (entropy increases), leading to a temperature decrease ($\Delta T < 0$) and heat absorption from the surroundings for refrigeration. In certain special circumstances, such as antiferroelectric (AFE) ceramics, the ECE behavior is reversed, namely a negative ECE: under adiabatic conditions, applying an electric field induces a temperature decrease ($\Delta T < 0$), corresponding to an entropy increase and heat absorption from the surroundings, whereas removing the electric field induces a temperature increase ($\Delta T > 0$), corresponding to an entropy decrease and heat release to the surroundings.[5]

The ECE was first discovered in Rochelle salt as early as the 1930s,[6] and it was not until the 1960s that FE materials became the primary focus of EC research. Early research mainly focused on bulk materials such as FE ceramics and single crystals, but the achieved EC performance was generally not satisfactory.[7] Among these materials, lead-based FE materials exhibited a large ECE of $\Delta T \approx 2.6$ K. In 2006, Mischenko *et al.*[8] prepared $PbZr_{0.95}Ti_{0.05}O_3$ thin films and achieved a giant ΔT up to 12 K by applying an ultrahigh electric field of 776 kV/cm, which directly triggered a surge of research in EC refrigeration. In 2008, Zhang *et al.*[9] prepared PVDF-based FE polymer thin films and achieved a giant ECE with $\Delta T_{max} = 12$ K. Beyond thin films, researchers also extended the sample thickness range to FE thick films with micrometer-scale thickness.[10–12] This approach aims to maintain a large refrigeration temperature change while increasing effective refrigeration volume, thereby yielding im-

†Corresponding author. E-mail: baiy@mater.ustb.edu.cn

© 2026 Chinese Physical Society and IOP Publishing Ltd. All rights, including for text and data mining, AI training, and similar technologies, are reserved.

proved practical refrigeration performance with higher cooling power. Over the past decade, researchers have conducted systematic investigations on FE materials, and have successively achieved groundbreaking giant ECE in various materials including ceramics, thin films, thick films, and polymers.[9–18] Research on the ECE has thus become a hot topic in the field of ferroelectrics.

While research on EC materials has advanced rapidly, the design of FE refrigeration devices has also made significant progress in recent years.[2–4,11,19–23] In 2017, Pei *et al.*[19] reported a high-efficiency micro EC refrigerator, which exhibited a refrigeration power of 2.8 W/g and a coefficient of performance (COP) of 13, far exceeding those of traditional and other new solid-state refrigeration solutions. In 2019, Mathuil *et al.*[11] reported a high ECE of up to 5.5 K in PST-MLCC. Based on this, the researchers successfully fabricated EC refrigeration devices, and achieved wide temperature span and large cooling power.[2–4] This advancement promoted EC refrigeration to the forefront of refrigeration technologies and paved a feasible path for its practical application.

2. Optimization of the EC performance

The ΔT of the ECE in FE materials can be described with the Maxwell relation, as shown below:

$$\Delta T = -\frac{T}{\rho C}\int_{E_1}^{E_2}\left(\frac{\partial P}{\partial T}\right)_E \mathrm{d}E, \tag{1}$$

where T, ρ and C are the temperature, density and specific heat of the material, respectively. E_1 and E_2 are the initial and the final electric field strengths, and $(\partial P/\partial T)_E$ is the pyroelectric coefficient at a certain electric field. According to the relations, the ECE is jointly determined by the electric field strength (E) and the pyroelectric coefficient $(\partial P/\partial T)_E$, and higher values of these two parameters contribute to a stronger ECE. The pyroelectric coefficient is mainly determined by the material composition, while the electric field strength is limited by the breakdown field, whose threshold value depends primarily on the material scale parameters and microstructural characteristics. In this chapter, we will illustrate, respectively, the optimization methods and the research progress of the ECE by increasing the electric field strength and/or the pyroelectric coefficient.

2.1. Enhancement of electric field strength

Before 2006, the ECE research primarily focused on bulk ceramics. However, the low breakdown field strength of bulk samples limited the achievable ΔT, making practical applications infeasible. As discussed above, the Maxwell relation indicates that the two key factors for enhancing the ΔT of the ECE are the pyroelectric coefficient and electric field strength. Since the operating electric field is limited by the material's dielectric strength, it is a critical factor in enhancing the breakdown field for improving EC performance. For FE dielectrics, the relationship between the breakdown field of material and the sample thickness can be expressed as follows:[24]

$$E_\mathrm{b} \propto d^{-n}\ [\mathrm{kV/cm}], \tag{2}$$

where E_b refers to the breakdown electric field, d is the thickness of the sample, and n is a fitting parameter determined by the microstructure and charge transfer.[25] Generally, bulk materials contain a large number of microscopic defects, which lead to a reduction in breakdown field strength, and the breakdown field strength is often only tens of kV/cm. Even if fabrication methods such as spark plasma sintering (SPS), hot-pressing sintering, or adding glass phase are adopted to improve the microstructure, the value of n can hardly decrease significantly, and the breakdown field strength of bulk samples can barely exceed 200 kV/cm. Therefore, significantly reducing the thickness of the dielectric layer is the most feasible solution to remarkably increase the breakdown field strength. The dimension of bulk samples is generally on the millimeter scale, while the thickness of thin films can reach the scale of tens to hundreds of nanometers, that is, the thickness can be reduced by 3 to 4 orders of magnitude. As a result, thin films have a higher operating electric field, which usually ranges from 600 kV/cm to 2000 kV/cm, and the corresponding ECE can reach 5 K–50 K. In recent years, the research on inorganic FE thin film materials has mainly focused on systems such as $Pb(Zr,Ti)O_3$,[26–28] $(Pb,La)(Zr,Ti)O_3$,[29] $Pb(Mg_{1/3}Nb_{2/3})O_3$-$PbTiO_3$ (PMN-PT)],[30–36] $PbZrO_3$,[37–39] $(Pb,Ba)ZrO_3$,[17] PST,[40–42] $SrBi_2Ta_2O_9$,[43] and others. For instance, Saranya *et al.*[30] reported that PMN-PT thin films near the morphotropic phase boundary (MPB) achieved a giant ECE with $\Delta T_\mathrm{max} = 31$ K at 140 °C under an electric field of 750 kV/cm. Hao *et al.*[18] fabricated $Pb_{0.97}La_{0.02}(Zr_{0.75}Sn_{0.18}Ti_{0.07})O_3$ (PLZST) AFE thin films, and obtained $\Delta T_\mathrm{max} = 53.8$ K under an electric field of 900 kV/cm.

Compared with bulk samples such as single crystals and ceramics, thin films can sustain a higher operating electric field, thereby resulting in a higher ΔT of the ECE. However, the effective volume of thin films is too small, which limits their actual heat absorption capacity and prevents them from meeting practical application requirements. Furthermore, due to the constraints of growth conditions, thin films are difficult to detach from substrates and exist independently. In addition, heat exchange between thin films and substrates significantly reduces their refrigeration efficiency. Therefore, thin films still face significant obstacles in moving toward practical applications. To address these issues, researchers have shifted their focus to ceramic thick film samples, particularly the MLCC structure, with the expectation of using multilayer ceramic thick films instead of thin films as the working medium for

FE refrigeration to achieve greater actual refrigeration capacity. On one hand, the thickness of ceramic thick films ranges from tens to hundreds of micrometers, and they can withstand ultra-high electric fields of hundreds of kV/cm for a similar giant ECE as the thin films. On the other hand, the effective volume of multilayer thick films is similar to that of bulk materials and much larger than that of thin films. Using the mature industrial MLCC process, the total number of layers of MLCC structured EC components can reach hundreds of layers. The huge effective volume enables an actual heat absorption capacity that is more than three orders of magnitude higher than that of thin films.

The multilayer thick films solution can effectively address the inherent drawbacks of the small effective volume of thin films and the low operating electric field of bulk materials. It is one of the preferred solutions for practical FE devices. Bai *et al.*[10] prepared $BaTiO_3$ (BT)-based MLCC thick films, and direct heat flux measurement results showed that the performance metrics of these multilayer thick films were comparable to those of thin films. For instance, they could withstand an ultrahigh electric field of 800 kV/cm and generate a high isothermal entropy change of 10.1 J/(kg·K) (corresponding to $\Delta T = 7.1$ K) at 80 °C. Mathur *et al.*[11] fabricated PST-MLCC, which achieved a giant ECE with $\Delta T_{\max} = 5.5$ K near room temperature under an electric field of 290 kV/cm. Bai *et al.*[12] designed an AFE $PbMg_{0.5}W_{0.5}O_3$ (PMW) MLCC, leveraging the spontaneous-chessboard-ordered structure of B-site heterovalent ions in PMW to achieve a large enthalpy change of 3.92 J/g. By combining the stress engineering of MLCCs (lowering the Curie temperature T_C to 19 °C) with the high dielectric strength of thin dielectric layers, they realized a giant positive and negative ECE, $\Delta T_{\max+} = 7.17$ K at 20 °C under 240 kV/cm and $\Delta T_{\max-} = -4.11$ K at 10 °C under 180 kV/cm below room temperature. Furthermore, the LCR oscillation circuit was employed for energy recovery, enabling a theoretical COP of 350 in the prototype refrigerator composed of 400 MLCCs. This work provides a critical solution for high-efficiency zero-emission refrigeration below room temperature. Therefore, high electric fields are a necessary condition for achieving the giant ECE, and MLCC structured EC components are the most promising solution.

2.2. Enhancement of the pyroelectric coefficient

The pyroelectric coefficient, on the other hand, is directly associated with a material's electric field-induced entropy change capability, and is another critical parameter determining the magnitude of ECE. Therefore, increasing the pyroelectric coefficient has become an important direction for enhancing ECE. With the development of EC refrigeration, a large number of studies at home and abroad have begun to focus on the design of EC materials based on FE phase transitions. FE materials with typical first-order phase transitions, such as BT, exhibit a huge peak value of ECE. Moya *et al.*[44] achieved an EC strength of $\Delta T/\Delta E = 0.22$ K·cm/kV in BT single crystals, while Bai *et al.*[45] achieved an ultrahigh EC strength of $\Delta T/\Delta E = 0.48$ K·cm/kV with defect-free BT single crystals. Although the first-order phase transition undergoes intense processes, its temperature range is narrow, resulting in a very narrow peak width of the ECE, which is only suitable for refrigeration applications within specific narrow temperature ranges. To meet broader application requirements, researchers have made phase transition more dispersed through ion substitution, aiming to further broaden the phase transition temperature range and regulate the phase transition temperature. Specifically, Bai *et al.*[46] prepared a series of $Ba_{1-x}Sr_xTiO_3$ ceramics ($x = 0.2$–0.4). By Sr substitution, they lowered the phase transition temperature to near room temperature and broadened the phase transition temperature range through phase transition dispersion. As the Sr content increases, the FE phase transition gradually becomes dispersed, and the peak of the ECE gradually broadens. Meanwhile, the peak value of ΔT decreases accordingly. When the Sr content is 35%, the ECE peak shifts to around room temperature, and the working temperature range is significantly broader than that of BT. Under an electric field of 20 kV/cm, they achieved a high ECE of $\Delta T_{\max} = 0.42$ K. Furthermore, they also investigated the effect of a series of rare earth element doping on the ECE of BT ceramics.[47] The results revealed that as the radius of the doped rare earth ions increases, the lattice tetragonality decreases, the polarization intensity weakens, the T_C gradually decreases, and the phase transition becomes more dispersed, resulting in a gradual broadening of the ECE peak but a corresponding decrease in the peak value of the ΔT. Among them, the $Ba_{0.94}Sm_{0.04}TiO_3$ ceramic could achieve a large ECE of $\Delta T_{\max} = 0.92$ K under an electric field of 30 kV/cm.

Effective ion doping can also induce new rhombohedral (R) or orthorhombic (O) phases in the original tetragonal (T) FE phase, forming multiphase coexistence regions or multiphase critical points (CP), namely, MPB and phase transition invariant points. The presence of multiple coexisting phase structures and complex physical mechanisms near the MPB facilitates phase transitions and yields excellent piezoelectric and FE properties. Therefore, the ECE of relaxor FE ceramics with MPB has attracted much attention. Bai *et al.*[48] prepared $Ba_{0.91}Ca_{0.09}Zr_{0.14}Ti_{0.86}O_3$ ceramics, tuning the ECE peak to around room temperature. Under an electric field of 20 kV/cm, they achieved excellent ECE with $\Delta T_{\max} = 0.33$ K and a full width at half maximum (FWHM) of 95 K. Zhang *et al.*[49] prepared $BaZr_{0.2}Ti_{0.8}O_3$ ceramics near the MPB, and added a glass phase to enhance the breakdown field strength. They obtained an outstanding ECE with $\Delta T_{\max} = 4.5$ K under an electric field of 145 kV/cm. In addition, they fabricated multilayer

thick films of the same composition, achieving a better ECE with $\Delta T_{max} = 7$ K under an electric field of 195 kV/cm.[50] Liu and Lou *et al.*[51] prepared Sn^{4+}-substituted BT ceramics. At the composition of $BaTi_{0.895}Sn_{0.105}O_3$, they realized the coexistence of R, O, T, and cubic (C) phases, and obtained an excellent ECE with $\Delta T_{max} = 0.61$ K. Similarly, Hf^{4+}-substituted BT ceramics can also achieve the coexistence of R, O, T, and C phases at the composition of $BaHf_{0.11}Ti_{0.89}O_3$.[52] Moreover, the multiphase coexistence point occurs around room temperature, exhibiting an excellent EC strength of $\Delta T/\Delta E = 0.035$ K·cm/kV.

In lead-based FE ceramics, the lead magnesium niobate-lead titanate (PMN-*x*PT) system has also attracted significant attention, particularly the MPB region where the PT content ranges from 28% to 35%. In 2015, Bai *et al.*[53] systematically investigated the ECE of PMN-*x*PT ceramics. The results showed that the PMN-*x*PT system exhibits multiple structural phase transitions, each of which leads to the emergence of an ECE peak. Moreover, the MPB region demonstrates the optimal polarization intensity and EC properties. When $x = 10$ or 25, the material undergoes a R–C phase transition, resulting in a single ECE peak. Within the MPB region at $x = 30$, 33, and 35, two ECE peaks were observed, corresponding to R–T and T–C phase transitions, respectively. Near the MPB, the material demonstrated a strong ECE and a broad phase transition temperature range, with $\Delta T_{max} = 0.60$ K under an electric field of 20 kV/cm. Rožič *et al.*[54] studied PMN-30PT FE ceramics. Via the direct measurement method, they obtained an excellent ECE with $\Delta T_{max} = 2.5$ K under an electric field of 90 kV/cm. This study also confirmed that the optimal EC strength can be achieved near the multiphase critical point.

3. Construction of multi-dimensional phase diagrams and the relationship with EC property

Many studies indicate that the ECE is closely associated with the FE phase transition. The regulation of phase composition and phase transition constitutes the core factor in enhancing EC performance, while the phase diagram of FE materials serves as an important basis for the design of EC properties. It is noteworthy that high electric fields are a necessary condition for generating usable EC refrigeration capacity, and the EC peak is always closely related to various FE phase transitions. However, previous design of FE materials only referred to the conventional composition–temperature phase diagrams, without considering the influence of external electric field on the phase transition. Since FE materials exhibit significant responses to various external field conditions, in addition to composition and temperature, external field stimuli such as electric field and stress can also induce changes in the crystalline structure of FE materials, i.e., triggering structural phase transitions. Currently, research on the ECE has gradually shifted from focusing only on the FE-paraelectric (PE) phase transition (i.e., the T_C) in the early stage of research to covering a variety of different phase transition types. For instance, these include transitions between FE phase and AFE phase, or between AFE phase and field-induced FE phase, transitions among different FE phases such as R–O–T, and even transitions between polar nano-regions (PNRs) in ergodic or non-ergodic states and long-range FE phases, etc. On the other hand, the intensity of the electric field applied in the ECE is becoming increasingly high. Under the action of a single electric field, materials with complex phase compositions near the MPB may even undergo multiple phase transition processes continuously. Therefore, the traditional composition-temperature phase diagram can no longer meet the current development requirements of ECE research. Instead, research on the ECE must take the multi-dimensional phase diagrams incorporating electric field conditions as the basis for material design.

The traditional methods of constructing phase diagrams mainly rely on analysis techniques such as *in-situ* transmission electron microscope (TEM), *in-situ* high-energy x-ray diffraction (XRD) and others. However, these characterization methods have high experimental requirements, and global experimental resources are scarce. Moreover, it is difficult to simultaneously meet experimental conditions of high temperature and high electric field, making it impossible to construct high-dimensional phase diagrams that incorporate electric fields. In recent years, by combining simple and convenient characterization methods such as *I–E* curves, *C–V* curves,[55–57] constant electric field heat flux measurement, constant electric field *P–T* and pyroelectric curves, we have been able to characterize the phase structure evolution behavior under the *E–T* coupled field conveniently and meticulously. These approaches can accurately locate the phase boundary positions and construct high-dimensional phase diagrams incorporating electric fields, thereby systematically revealing the FE behavior characteristics of materials under the multi-physics coupling conditions of electric field and temperature. In this chapter, by constructing *E–T* phase diagrams, we conducted systematic analysis on the ECE of FE single crystals, relaxor FE ceramics, and AFE ceramics respectively.

3.1. PMN-PT single crystals

As one of the most well-studied FE materials, PMN-PT has a complex phase transition process with either temperature or electric fields and versatile EC properties. The microscopic phase evolution within MPB is not clear completely and its relationship with macroscopic FE properties including the EC property also needs to be clarified. Constructing *E–T* phase diagrams for PMN-PT single crystals well bridges mi-

croscopic crystalline characteristics and macroscopic FE properties, and it also demonstrates how to provide detailed physical understanding of the EC mechanisms from a microscopic view.

To address these unresolved issues and leverage E–T phase diagrams as a micro-macro bridge, Li *et al.*[58] analyzed the ECE of PMN-PT single crystals through high-dimensional phase diagrams. They integrated dielectric, polarization, and pyroelectric data to characterize phase behavior of ⟨001⟩, ⟨011⟩, and ⟨111⟩-oriented 0.7Pb($Mg_{1/3}Nb_{2/3}$)O_3-0.3$PbTiO_3$ (PMN-30PT) single crystals (Fig. 1). They identified and extracted the critical characteristic points of phase transitions under different electric fields and temperatures, and marked them in the E–T coordinate space using spherical, square, and star-shaped symbols, respectively. Based on the principle that the critical electric field of phase transition decreases linearly with increasing temperature, linear fitting was performed on these critical points to determine the

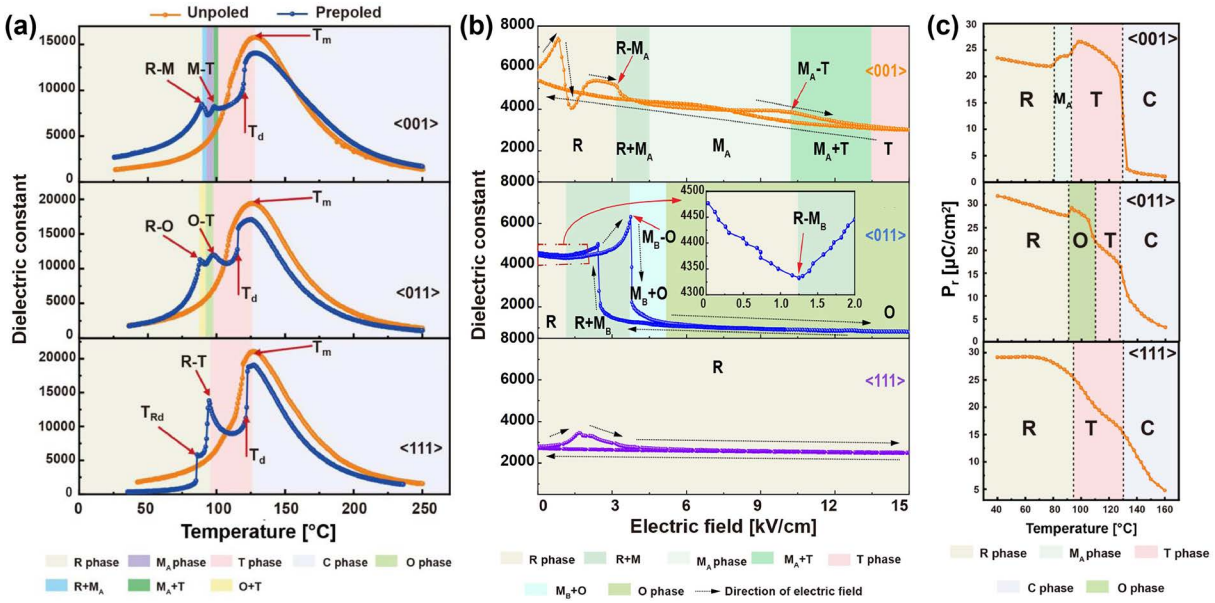


Fig. 1. The phase-related physical properties of ⟨001⟩, ⟨011⟩, ⟨111⟩-oriented PMN-30PT single crystals: (a) dielectric–temperature (ε–T) curves, (b) dielectric–electric field (ε–E) curves, (c) remanent polarization–temperature (P_r–T) curves. Reproduced with permission from Ref. [58] from Elsevier, Copyright 2020.

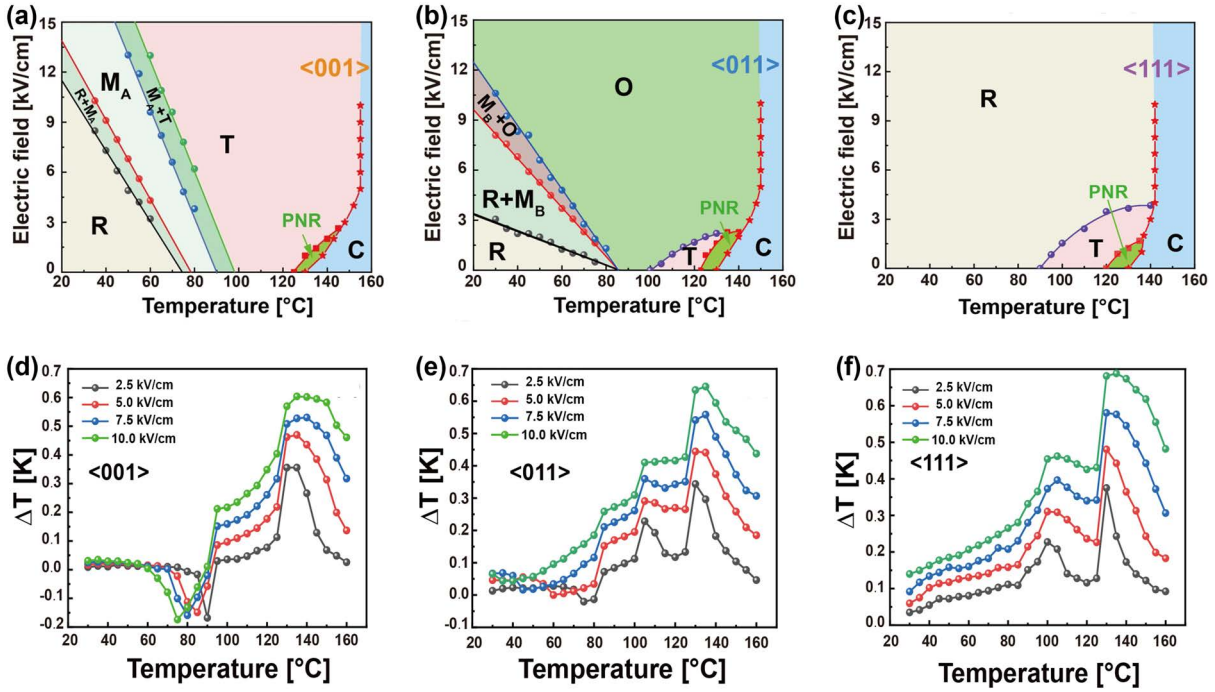


Fig. 2. The E–T phase diagram and ECE of different oriented PMN-30PT single crystals. E–T phase diagram of (a) ⟨001⟩, (b) ⟨011⟩, (c) ⟨111⟩-oriented PMN-30PT single crystals. The sphere symbols are experimental points obtained from the $\varepsilon(E)$ curves, the square symbols from the polarization current curves, and the star symbols from the pyroelectric coefficient. Temperature dependence of the ECE ΔT for (d) ⟨001⟩, (e) ⟨011⟩, (f) ⟨111⟩-oriented PMN-30PT single crystals. Reproduced with permission from Ref. [58] from Elsevier, Copyright 2020.

boundary lines between adjacent phase regions. Finally, according to the phase boundaries, in combination with the structural characteristics and physical responses of each phase region, the E–T space was divided into distinct phase regions, thereby completing the construction of the phase diagram (Figs. 2(a)–2(c)). The phase diagrams reveal distinct orientation-dependent complexity. The ⟨001⟩-oriented crystals show seven phase regions and six core sequential phase transition processes, the ⟨011⟩-oriented ones exhibit intermediate phase coexistence and temperature-electric field competition, while the ⟨111⟩-oriented crystals have simplified transitions, reflecting that crystal orientation dominates phase evolution pathways.

These E–T phase diagrams further decode the tailored ECE responses of differently oriented PMN-30PT single crystals under electric-thermal coupling (Fig. 2). The ⟨001⟩-oriented crystals show segmented ECE (weak positive-negative-positive), the ⟨011⟩-oriented ones switch from negative to positive ECE with increasing electric field, while the ⟨111⟩-oriented crystals maintain positive ECE due to aligned electric field and R phase polarization. A critical conclusion is that crystal symmetry, phase transition paths, and entropy change behavior synergistically govern ECE sign and amplitude. Non-⟨111⟩ orientations introduce phase competition, leading to tunable ECE signs, while ⟨111⟩ orientation stabilizes positive ECE. This work highlights the core value of E–T phase diagram in bridging microscopic phase evolution and macroscopic EC performance, providing a rigorous paradigm for targeted ECE optimization in FE single crystals.

3.2. Relaxor FE ceramics

Relaxor FE ceramics are currently a research hotspot in the field of FE materials. Their unique characteristics, such as strong polarization and smooth temperature change, are conducive to obtaining excellent EC performance for practical applications. While the PNRs endow them with different characteristics of polarization variation from the normal FE phase transition under the coupling effect of temperature and electric fields. An in-depth exploration of their physical mechanism also cannot be separated from the E–T phase diagram.

Responding to this imperative for E–T phase diagram-driven mechanism exploration, Bobnar *et al.*[59] focused on the 9/65/35 lead lanthanum zirconate titanate (PLZT) relaxor FE ceramics. They constructed E–T phase diagrams via three dielectric measurement approaches, clarifying phase boundaries of the ergodic relaxor (ER) phase, non-ergodic relaxor (NR) phase, and long-range FE phase, as well as the path dependence of phase transitions and the characteristics of transition lines. Beyond filling the research gap in the relevant field and guiding applications, it validates dielectric multi-dimensional characterization as a reliable tool for decoding relaxor mechanisms, laying a foundation for similar studies.

Building on this, the previous studies systematically analyzed the ECE evolution and mechanisms of $Pb_{0.91}La_{0.06}Zr_{0.8}Ti_{0.2}O_3$ (PLZT) relaxor FE ceramics by constructing a multi-dimensional phase diagram of E–T coupling,[60] as shown in Fig. 3. The phase transition behavior and the evolution of the ECE of PLZT relaxor FE ceramics exhibit significant E–T coupling dependence, showing three typical response regions bounded by depolarization temperature T_d and maximum dielectric constant temperature T_m. Under medium-to-high electric fields, the low and high-temperature regions exhibit ECE peaks, while the medium-temperature region features a broad ECE platform. Notably, the electric field-induced transition from short-range ordered PNRs to long-range ordered FE macrodomains can induce a more significant ECE compared to processes involving only the reorientation of FE macrodomains or PNRs alone. This medium-temperature ECE platform provides crucial support for the design of wide-temperature-range solid-state refrigeration devices, bridging fundamental phase mechanisms and practical application needs.

To further expand the exploration of ECE mechanisms and phase diagram construction across diverse relaxor FE systems, Weyland *et al.*[61] focused on three bismuth sodium titanate (NBT)-based relaxor FEs, namely, 0.94 $(Na_{1/2}Bi_{1/2}TiO_3)$-0.06 $(BaTiO_3)$ (NBT-BT), 0.80 $(Na_{1/2}Bi_{1/2}TiO_3)$-0.20 $(K_{1/2}Bi_{1/2}TiO_3)$ (NBT-KBT), and 0.75 $(Na_{1/2}Bi_{1/2}TiO_3)$-0.25 $(SrTiO_3)$ (NBT-ST). They integrated dielectric constant, thermometry, and phase transition latent heat (via c_p calculation) measurements to characterize E–T coupled phase behavior and construct detailed E–T phase diagrams (Fig. 4). The phase diagrams delineate NR, ER, and field-induced FE phase regions, mark first-order/reverse transition lines and CP, and reveal electric field hysteresis that diminishes with temperature and vanishes at CP. The three materials exhibit distinct CP parameters. NBT-KBT exhibits a wider temperature range for reversible phase transitions, while NBT-ST is in the ER phase at room temperature. This work decodes the phase rules of NBT-based relaxor FEs, and provides direct guidance for selecting operating ranges in electromechanical and EC applications, further confirming the irreplaceable role of E–T phase diagram in decoding PNR-related polarization mechanisms.

Collectively, these studies consistently take the E–T phase diagram as the core tool to explore the intrinsic links PNR-dominated polarization variations, phase transition behaviors, and ECE performance. The unique PNR-derived properties of relaxor FE ceramics are the key to their excellent EC performance, and E–T phase diagrams are indispensable for decoding physical mechanisms.

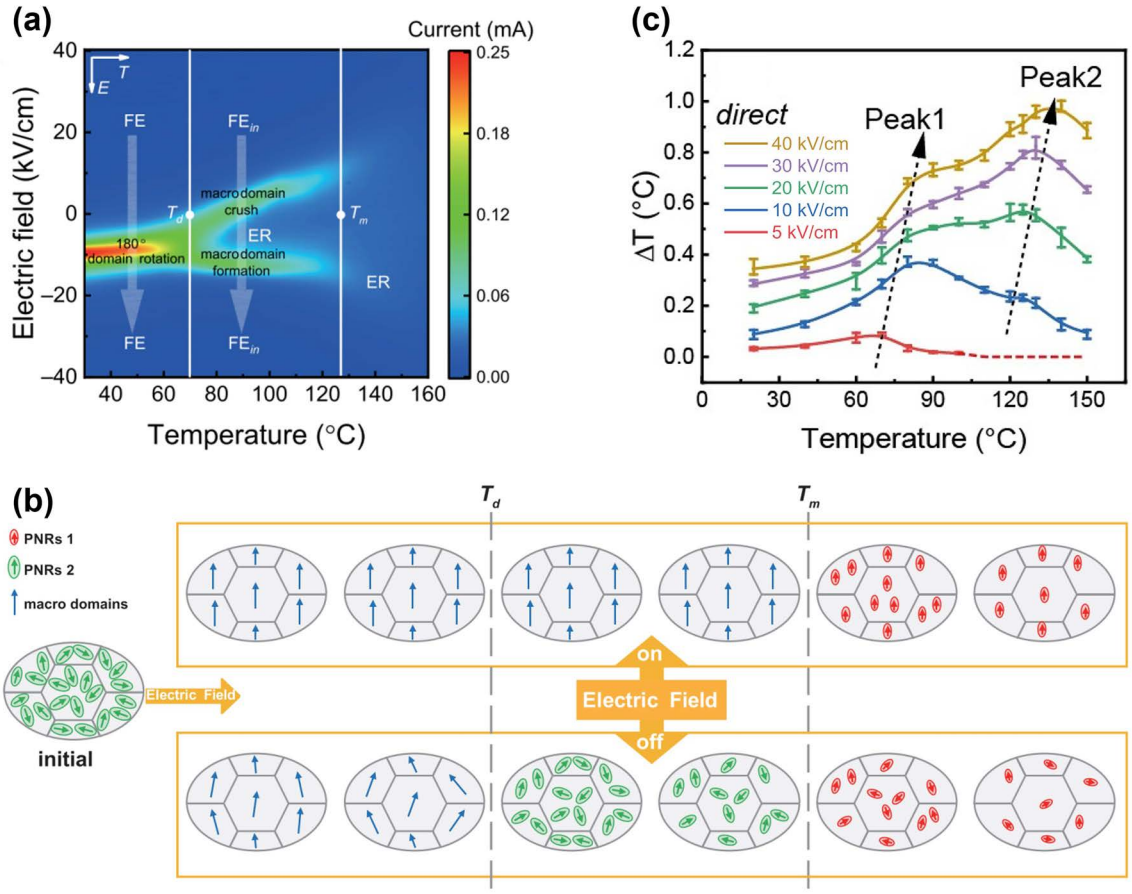


Fig. 3. The E–T phase diagram and the mechanism of ECE in PLZT relaxor FE ceramics. (a) The E–T phase diagram. (b) Schematic illustration of the domain evolution processes for PLZT relaxor ceramics under coupling of electric field and temperature. PNRs 1 ($T < T_m$) are frozen and static, whereas PNRs 2 ($T > T_m$) are highly dynamic. (c) Temperature dependence of ΔT under different electric fields by direct isothermal heat flow measurement. Reproduced with permission from Ref. [60] from APS, Copyright 2019.

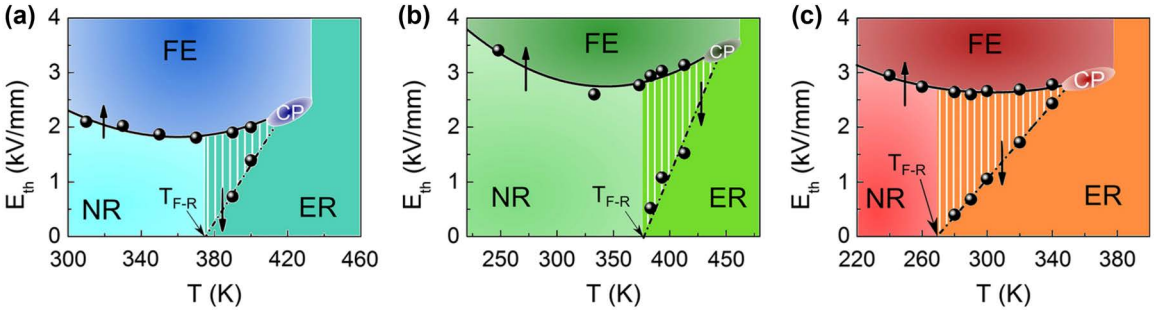


Fig. 4. The E–T phase diagram with stability regions of (a) NBT-BT, (b) NBT-KBT, (c) NBT-ST. The critical point is abbreviated as CP and included as an area due to the smearing of critical parameters caused by heterogeneity of the crystallographic orientations in ceramics.[62,63] Arrows denote whether the electric field was increased (up) or decreased (down). Reproduced with permission from Ref. [61] from Springer Nature, Copyright 2018.

3.3. AFE ceramics

The microscopic dipoles in AFE materials are arranged antiparallelly, while those in FE materials are arranged parallelly. Which of the two has a higher dipole order entropy, and how the dipole ordering entropy changes during the phase transition has always been a mystery that puzzled researchers in the field of ECE. The E–T phase diagrams provide a powerful tool for clarifying the above issues.

Tracking the scarce research on the AFE–FE phase boundary and unraveling the mystery of dipole ordering entropy, Li *et al.*[5] designed a new ceramic system $Pb_{0.97-x}Ba_xLa_{0.02}Zr_{0.95}Ti_{0.05}O_3$, namely, PBLZT100$x$, by incorporating Ba^{2+} into orthogonal antiferroelectric (AFE_O) ceramics, successfully constructing a MPB between AFE_O and rhombohedral ferroelectric (FE_R) phases. They analyzed the ECE microscopic mechanism of PBLZT4 (near the AFE end of the MPB) via high-dimensional E–T phase diagrams (Fig. 5), revealing that the AFE–FE critical electric field increases with temperature, and the material exhibits segmented ECE (negative in medium-temperature, positive in

high-temperature regions). The E–T phase diagram further reveals that the positive and negative ECE originate from the field-induced cubic PE-low-temperature FE_R phase transition and the field-induced AFE_O-high-temperature FE_R phase transition, respectively. Landau calculations confirmed the most significant EC entropy change occurs during these transitions, and the triple CP of AFE_O–FE_R–PE with low energy barriers enables the coexistence of large positive and negative ECE. This discovery highlights the deterministic role of entropy change differences near phase boundaries in regulating the sign and amplitude of EC responses, providing an important phase diagram-based basis for the regulation of the ECE in AFE ceramic systems.

Leveraging the phase diagram-driven ECE insights gleaned from PBLZT ceramics, Li *et al.*[64] extended the research to a classic AFE ceramic system, $Pb_{0.99}Nb_{0.02}[(Zr_{0.6}Sn_{0.4})_{1-x}Ti_x]_{0.98}O_3$ (PNZST100x), to explore the relationship between phase diagram characteristics and ECE performance. They constructed E–T phase diagrams via current density–electric field (J–E) curves (Fig. 6), clarifying phase regions, boundaries, and transition types, and the multiphase coexistence CP of tetragonal AFE (AFE_T), FE_R, and multicell/single-cell cubic PE (PE_{MCC}/PE_{SCC}) phase. Systematic investigation of compositions near the CP showed that the composition with $x = 0.08$ exhibits the most complex ECE evolution due to its abundant phase transitions. A key finding is that phase boundary slope dictates dipole order entropy change direction and thus the sign and magnitude of ECE. Positive slopes correspond to field-driven AFE_T–FE_R transition (antiparallel–parallel dipoles, entropy decrease), inducing large positive ECE. While negative slopes relate to AFE_T–PE_{MCC} transition (antiparallel–disordered dipoles, entropy increase), triggering significant negative ECE. This confirms phase region distribution and boundary features are core regulators of ECE diversity. Ceramics in the AFE_T phase region exhibit both positive and negative ECE (dual entropy change paths), while those in the FE_R and PE phase regions only exhibit positive ECE (single entropy decrease path), providing clear theoretical and experimental basis for the targeted design of high-performance EC materials.

However, a critical bottleneck emerged after clarifying the E–T phase diagrams of PBLZT and PNZST AFE ceramics. Due to either the phase transition temperature deviating from room temperature or insufficient phase region symmetry, both are difficult to meet the requirement for large ECE performance at room temperature. Against this backdrop, PMW AFE ceramics, endowed with the advantage of ionic ordering via the B-site high valence difference, provide a new solution for overcoming this limitation, making the intrinsic correlation between their E–T phase diagrams and ECE a key research direction.

To explore the potential of PMW AFE ceramics for room-temperature large ECE performance, Li *et al.*[65] systematically investigated the correlation mechanism between the E–T phase diagram and ECE based on ε–E curves at different temperatures (a typical curve is shown in Fig. 7(a)). They constructed an E–T phase diagram via dielectric constant contour plots (Fig. 7(b)), delineating the low-temperature AFE, high-temperature PE, and field-induced FE phase. This phase diagram exerts a significant regulatory role on EC performance (Fig. 7(c)), it reveals that PMW exhibits room-temperature-targeted ECE. Below the T_C (36 °C), the field-induced AFE_O-high-temperature FE phase (with a negative phase boundary slope), accompanied by microstructure evolution, yields a negative ECE ($\Delta T_{max} = -2.02$ K at 34 °C). Above T_C, field-induced cubic PE-low-temperature FE phase (with a positive phase boundary slope) generates a positive ECE ($\Delta T_{max} =$ 1.79 K at 36 °C). Notably, increasing the electric field shifts the phase transition peak toward lower temperatures, while incompletely driven electric field-induced phase transitions limit further enhancement of ECE. This phase diagram provides crucial theoretical support for in-depth analysis of the ECE generation mechanism and precise optimization of the material's EC performance.

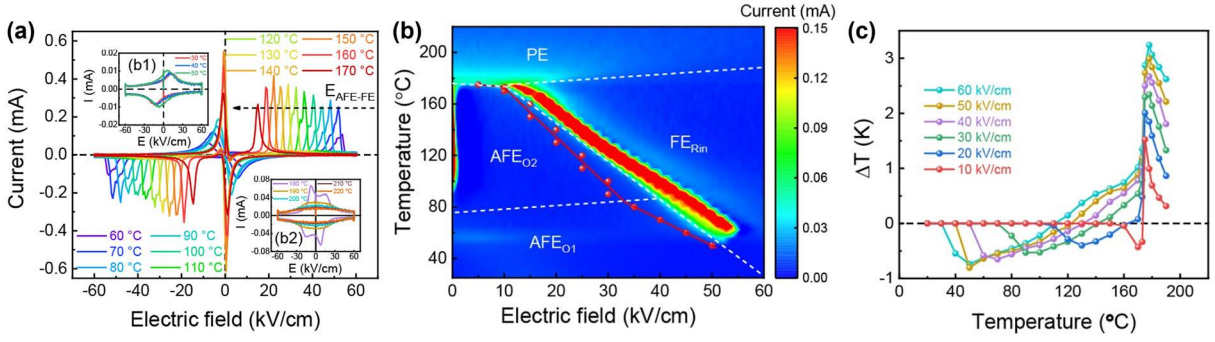


Fig. 5. The E–T phase diagram and ECE in PBLZT4 AFE ceramics. (a) I–E curves at different temperatures. (b) The E–T phase diagram determined via temperature-dependent I–E curves. The red band depicts the peaks of I–E curves, and the red line stands for the electric fields of the maximum negative ECEs. White dotted lines stand for the boundaries between different phases. (c) ECE ΔT as a function of temperature under different electric fields measured using a modified differential scanning calorimeter. Reproduced with permission from Ref. [5] from American Chemical Society, Copyright 2020.

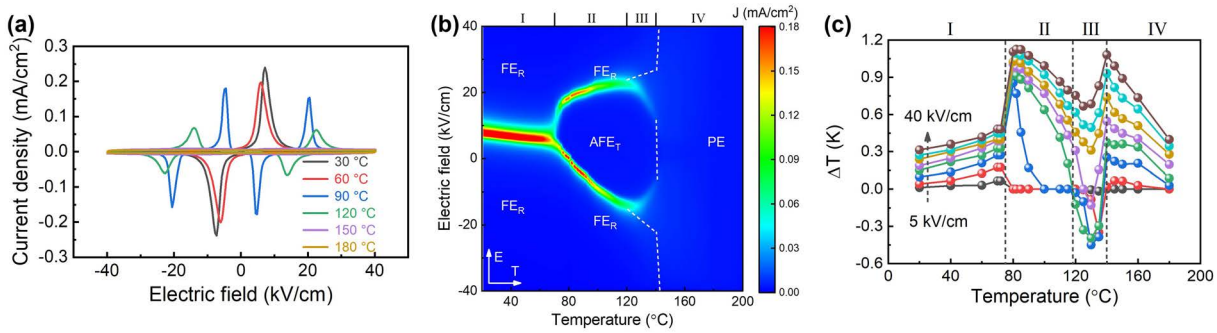


Fig. 6. The E–T phase diagram and ECE in PNZST8 ceramics. (a) Contour mappings of J with varying temperatures and electric fields. (b) ΔT–T curves under different electric fields. Reproduced with permission from Ref. [64] from Tsinghua University Press, Copyright 2021.

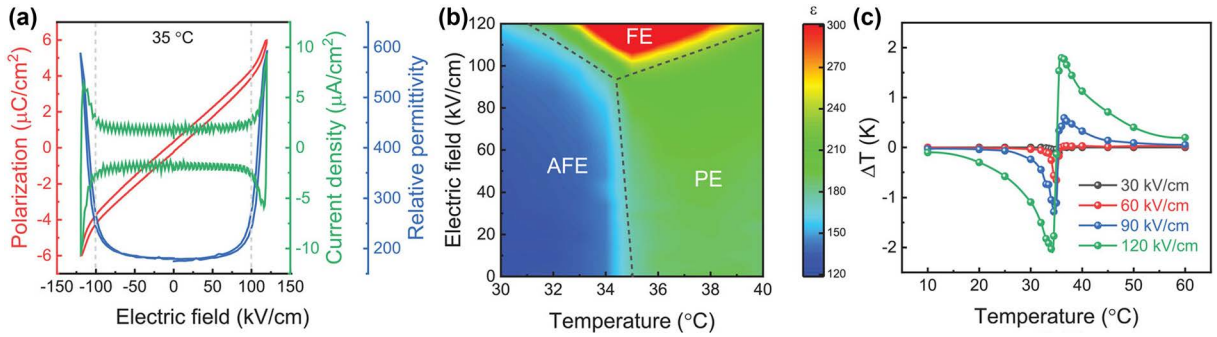


Fig. 7. The E–T phase diagram and ECE in PMW ceramics. (a) The electric field dependence of polarization, current density, and relative permittivity at 35 °C. (b) Contour plots of the ε–E curves under different temperatures. (c) ECE ΔT as a function of temperature under different electric fields from 10 °C to 60 °C. Reproduced with permission from Ref. [65] from Wiley, Copyright 2021.

Taken together, the studies on PBLZT, PNZST, and PMW systems with E–T phase diagrams as the core tool elucidate the dipole order entropy evolution in AFE–FE materials. The direction of dipole order entropy change is determined by phase transition pathways. Transitions from high-entropy states (disordered random dipole orientations or antiparallel ordered orientation, typical of AFE phases) to low-entropy parallel ordered dipole orientations (typical of FE phases) induce an entropy decrease ($\Delta S < 0$), which corresponds to a positive ECE. While transitions from medium-entropy antiparallel ordered states (AFE phases) to high-entropy disordered random dipole orientations (PE phases) lead to an entropy increase ($\Delta S > 0$), which corresponds to a negative ECE. Meanwhile, phase boundary characteristics and crystal orientation indirectly tune the magnitude of entropy change by regulating phase transition pathways. Evidently, E–T phase diagrams provide robust theoretical guidance and lay a crucial research foundation for targeted development of high-performance AFE–FE EC materials.

3.4. BT single crystals by simulation

As the most typical FE material, BT not only has numerous experimental results but is also the object that researchers have conducted the most computational simulations on. By establishing E–T phase diagrams based on simulation data, it is possible to describe the microscopic features and dynamic evolution processes that are difficult to achieve in experiments, thereby gaining a deeper understanding of its physical mechanism.

Addressing the scarcity of research on EC behaviors under arbitrary electric field directions (a gap compared to studies on high-symmetry orientations and field intensity effects of FE materials[53,58,66–74]), the research team targeted BT single crystals. They employed the molecular dynamics simulation based on a first-principles-based effective Hamiltonian, combined with the Landau–Devonshire phenomenological theory, to systematically investigate the phase transition process and ECE characteristics under electric field applied along 11 specific directions within three crystallographic planes (001), $(\bar{1}10)$, and $(0\bar{1}1)$.[75] Based on P–T curves, a three-dimensional phase diagram integrating electric field direction-electric field strength-temperature was constructed, as shown in Figs. 8(a)–8(c). When the electric field aligns collinearly with the spontaneous polarization direction of the FE phase, the FE phase retains its original phase structure, while non-collinear orientations induce lattice distortion and transform the FE phase into a low-symmetry monoclinic phase. As shown in Figs. 8(d)–8(f), three ECE peaks across the temperature range correspond to distinct phase transitions. The T–C phase transition shows positive ECE with peak intensity/width dependent on the field-polarization angle. The O–T and R–O phase transitions show sign switching from positive to negative as the electric field rotates between FE crystallographic orientations. Under specific low-symmetry electric

field directions, the coexistence of positive and negative ECE can occur during the same phase transition. Overall, the electric field orientation regulates phase transition symmetry via phase diagram boundaries, directly determining the positive or negative sign, intensity, and peak position of ECE.

Building on the phase diagram-based insights into ECE regulation by electric field orientation, Li *et al.*[76] further explored the influence of thermoelectric history on the ECE of BT single crystals via molecular dynamics simulations. It was found that all three first-order phase transitions of the material exhibit a maximum thermal hysteresis region under zero electric field, which gradually shrinks and vanishes with increasing electric field strength. The reversibility of ECE is jointly governed by temperature, electric field history, and intensity. Irreversible phase transition and ECE occur when either the initial or final state of electric field variation lies within the hysteresis region (with significant ECE only during the first electric field variation and weak responses thereafter), while reversible behavior emerges when both states cross the hysteresis region. Regardless of positive or negative ECE, electrical hysteresis loss causes a gradual increase in the system's temperature baseline under continuous electric field cycling. This confirms thermoelectric history governs ECE reversibility and stability, clarifying the coupling between hysteresis and ECE and providing critical guidance for optimizing electric field cycling strategies and avoiding irreversible losses in high-performance refrigeration cycle design.

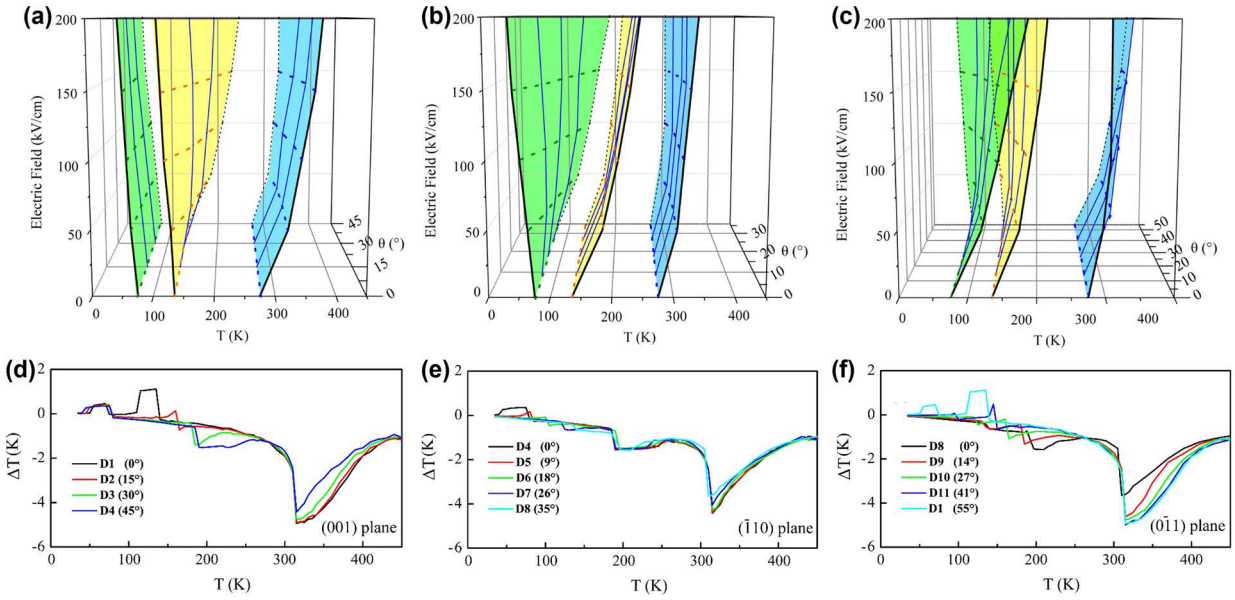


Fig. 8. Electric field direction–electric field strength–temperature (θ–E–T) phase diagrams and ECE in different crystallographic planes of BT single crystals. θ–E–T in (a) (001) plane, (b) ($\bar{1}$10) plane and (c) (0$\bar{1}$1) plane. ECE ΔT as a function of temperature during the removal of the electric field from 200 kV/cm to 0 kV/cm along directions in (d) (001) plane, (e) ($\bar{1}$10) plane and (f) (0$\bar{1}$1) plane. Reproduced with permission from Ref. [75] from Elsevier, Copyright 2020.

Overall, these studies on BT single crystals take E–T phase diagrams based on simulation data as the core tool to decipher microscopic phase dynamics and their correlation with macroscopic ECE performance. From analyzing orientation-dependent ECE characteristics to clarifying thermoelectric history effects, they fully illustrate that E–T phase diagrams are indispensable for revealing the physical mechanisms of BT that are hard to capture via experiments.

4. Conclusion and outlook

FE materials show promising application prospects in the field of EC refrigeration technology, with their ferroelectricity intricately linked to phase transition behaviors under high electric fields. Constructing multi-dimensional phase diagrams incorporating electric field variables has become a core method for analyzing the microstructure–property relationships of these materials. Through the comprehensive analysis of dielectric, polarization, pyroelectric, and other performance characteristics under multi-field coupling conditions, multi-dimensional phase diagrams can directly correlate the microscopic phase transition paths (such as the evolution of PNRs and phase boundary migration) with the macroscopic EC response, providing theoretical guidance for the targeted design of high-performance FE materials. By regulating composition and electric field based on the multi-dimensional phase diagrams, the high entropy change characteristics of first-order phase transitions and the wide temperature range advantages of diffuse phase transitions can be effectively achieved simultaneously, which will also facilitate the innovations in EC material design.

The future research on the design of EC materials based on FE phase diagrams will focus on the following ar-

eas. (i) The integration of data-driven methods and high-throughput computing to accelerate the large-scale construction of FE phase diagrams, achieving a paradigm shift in material design from "empirical trial-and-error" to efficient "phase diagram-guided" strategies. (ii) The combination of multi-physics *in-situ* characterization techniques and dynamic phase diagrams to reveal the real-time evolution and mechanisms of ECE in complex operating environments. (iii) The collaborative innovation of EC refrigeration materials and micro-device structures, precisely locating optimal operating regions through phase diagrams, and advancing the practical application of FE refrigeration technology in fields such as microelectronics heat dissipation. With the continued development of interdisciplinary research, FE refrigeration systems guided by multi-dimensional phase diagrams will provide critical solutions for the next generation of solid-state refrigeration technology.

Acknowledgments

Project supported by the National Natural Science Foundation of China (Grant Nos. U25A20232, 52325208, 52173217, and 52202128) and the Interdisciplinary Research Project for Young Teachers of USTB (Grant No. FRF-IDRY-24-002).

References

[1] Han D L, Zhang Y J, Huang C L, Zheng S Y, Wu D Y, Li Q, Du F H, Duan H X, Chen W L, Shi J Y, Chen J P, Liu G, Chen X and Qian X S 2024 *Nature* **629** 1041
[2] Li J N, Torelló A, Kovacova V, Prah U, Aravindhan A, Granzow T, Usui T, Hirose S and Defay E 2023 *Science* **382** 801
[3] Wang Y D, Zhang Z Y, Usui T, Benedict M, Hirose S, Lee J, Kalb J and Schwartz D 2020 *Science* **370** 129
[4] Torelló A, Lheritier P, Usui T, Nouchokgwe Y, Gérard M, Bouton O, Hirose S and Defay E 2020 *Science* **370** 125
[5] Li J J, Li J T, Wu H H, Qin S Q, Su X P, Wang Y, Lou X J, Guo D, Su Y J, Qiao L J and Bai Y 2020 *ACS Appl. Mater. Interfaces* **12** 45005
[6] Kobeco P and Kurtchatov I 1930 *Z. Phys* **66** 192
[7] Hegenbarth E 1961 *Cryogenics* **1** 242
[8] Mischenko A S, Zhang Q, Scott J, Whatmore R W and Mathur N D 2006 *Science* **311** 1270
[9] Neese B, Chu B J, Lu S G, Wang Y, Furman E and Zhang Q M 2008 *Science* **321** 821
[10] Bai Y, Zheng G P, Ding K, Qiao L J, Shi S Q and Guo D 2011 *J. Appl. Phys.* **110** 094103
[11] Nair B, Usui T, Crossley S, Kurdi S, Guzmán-Verri G G, Moya X, Hirose S and Mathur N D 2019 *Nature* **575** 468
[12] Yin R W, Liu D, Lv X W, Jiao K L, Hou Y X, Li J J, Luo H J, Zhong R J, Qi X Y, Liu C B, Su Y J, Qiao L J, Che R C, Zhu L F, Lookman T and Bai Y 2025 *Adv. Funct. Mater.* **35** 2502550
[13] Du F H, Yang T N, Hao H, *et al.* 2025 *Nature* **640** 924
[14] Yin R W, Hou Y X, Lv X W, Li J J, Zhong R J, Su Y J, Qiao L L, Che R C, Zhu L F, Liu C B and Bai Y 2025 *J. Adv. Ceram.* **14** 9221088
[15] Zheng S Y, Du F H, Zheng L R, Han D L, Li Q, Shi J Y, Chen J P, Shi X M, Huang H B, Luo Y R, Yang Y R, O'reilly P, Wei L L, Souza N D, Hong L and Qian X S 2023 *Science* **382** 1020
[16] Qian X S, Han D L, Zheng L R, *et al.* 2021 *Nature* **600** 664
[17] Peng B L, Fan H Q and Zhang Q 2013 *Adv. Funct. Mater.* **23** 2987
[18] Zhao Y, Hao X H and Zhang Q 2015 *J. Mater. Chem. C* **3** 1694
[19] Ma R J, Zhang Z Y, Tong K, Huber D, Kornbluh R, Ju Y S and Pei Q B 2017 *Science* **357** 1130
[20] Bo Y W, Zhang Q, Cui H, Wang M Y, Zhang C Y, He W, Fan X Q, Lv Y W, Fu X and Liang J J 2021 *Adv. Energy Mater.* **11** 2003771
[21] Meng Y, Zhang Z Y, Wu H X, Wu R Y, Wu J H, Wang H L and Pei Q B 2020 *Nat. Energy* **5** 996
[22] Schader F H, Isaia D, Weber M, Aulbach E and Webber K G 2018 *J. Mater. Sci.* **53** 3296
[23] Webber K, Aulbach E, Key T, Marsilius M, Granzow T and Rödel J 2009 *Acta Mater.* **57** 4614
[24] Yoshimura M and Bowen H 1981 *J. Am. Ceram. Soc.* **64** 404
[25] Forlani F and Minnaja N 1964 *Physica Status Solidi* **4** 311
[26] Chukka R, Cheah J W, Chen Z H, Yang P, Shannigrahi S, Wang J L and Chen L 2011 *Appl. Phys. Lett.* **98** 242902
[27] Boni G A, Filip L D, Radu C, Chirila C, Pasuk I, Botea M, Pintilie I and Pintilie L 2022 *Electron. Mater.* **3** 344
[28] Bag S P, Hou X, Zhang J T, Wu S H and Wang J 2020 *IEEE Trans. Electron Devices* **67** 1769
[29] Hao X H, Yue Z X, Xu J B, An S L and Nan C W 2011 *J. Appl. Phys.* **110** 064109
[30] Saranya D, Chaudhuri A R, Parui J and Krupanidhi S B 2009 *Bull. Mater. Sci.* **32** 259
[31] Lu S G, Rožič B, Zhang Q M, Kutnjak Z, Li X Y, Furman E, Gorny L J, Lin M R, Malič B and Kosec M 2010 *Appl. Phys. Lett.* **97** 162904
[32] He Y, Li X M, Gao X D, Leng X and Wang W 2011 *Funct. Mater. Lett.* **4** 45
[33] Feng Z Y, Shi D Q and Dou S X 2011 *Solid State Commun.* **151** 123
[34] Feng Z Y, Shi D Q, Zeng R and Dou S X 2011 *Thin Solid Films* **519** 5433
[35] Mischenko A S, Zhang Q, Whatmore R W, Scott J F and Mathur N D 2006 *Appl. Phys. Lett.* **89** 242912
[36] Correia T, Young J, Whatmore R W, Scott J, Mathur N and Zhang Q 2009 *Appl. Phys. Lett.* **95** 182904
[37] Parui J and Krupanidhi S B 2008 *Phys. Status Solidi RRL* **2** 230
[38] Yuan Y, Sun B W, Guo M Y, Wu M, Gao Y F, Zhu X P, Sun H N, Zhao J T, Liu Y B and Gao J H 2022 *J. Alloys Compd.* **899** 163165
[39] Liang Y X, Li W H, Jian Z F, Song W L, Zhao R K, Tang X G, Jiang Y P, Guo X B and Yan K 2025 *Colloid Surf. Physicochem. Eng. Asp.* **709** 136138
[40] Correia T M, Kar-Narayan S, Young J S, Scott J F, Mathur N D, Whatmore R W and Zhang Q 2011 *J. Phys. D: Appl. Phys.* **44** 165407
[41] Kovacova V, Glinsek S, Girod S and Defay E 2022 *Sensors* **22** 4049
[42] Aravindhan A, Glinsek S, Girod S, Martinez A B, Granzow T, Kovacova V and Defay E 2024 *Heliyon* **10** e30430
[43] Chen H, Ren T L, Wu X M, Yang Y and Liu L T 2009 *Appl. Phys. Lett.* **94** 182902
[44] Moya X, Stern-Taulats E, Crossley S, González-Alonso D, Kar-Narayan S, Planes A, Mañosa L and Mathur N D 2013 *Adv. Mater.* **25** 1360
[45] Bai Y, Han X, Zheng X C and Qiao L J 2013 *Sci. Rep.* **3** 2895
[46] Bai Y, Han X, Ding K and Qiao L J 2013 *Appl. Phys. Lett.* **103** 162902
[47] Han F, Bai Y, Qiao L J and Guo D 2016 *J. Mater. Chem. C* **4** 1842
[48] Bai Y, Han X and Qiao L J 2013 *Appl. Phys. Lett.* **102** 252904
[49] Qian X S, Ye H J, Zhang Y T, Gu H M, Li X Y, Randall C and Zhang Q M 2014 *Adv. Funct. Mater.* **24** 1300
[50] Ye H J, Qian X S, Jeong D Y, Zhang S J, Zhou Y, Shao W Z, Zhen L and Zhang Q M 2014 *Appl. Phys. Lett.* **105** 152908
[51] Luo Z D, Zhang D W, Liu Y, Zhou D, Yao Y G, Liu C Q, Dkhil B, Ren X B and Lou X J 2014 *Appl. Phys. Lett.* **105** 102904
[52] Li J N, Zhang D W, Qin S Q, Li T Y, Wu M, Wang D, Bai Y and Lou X J 2016 *Acta Mater.* **115** 58
[53] Bai Y, Wei D and Qiao L J 2015 *Appl. Phys. Lett.* **107** 192904
[54] Rožič B, Kosec M, Uršič H, Holc J, Malič B, Zhang Q M, Blinc R, Pirc R and Kutnjak Z 2011 *J. Appl. Phys.* **110**
[55] Bolten D, Böttger U and Waser R 2003 *J. Appl. Phys.* **93** 1735
[56] Bolten D, Böttger U and Waser R 2004 *J. Eur. Ceram. Soc.* **24** 725
[57] Bolten D, Lohse O, Grossmann M and Waser R 1999 *Ferroelectrics* **221** 251
[58] Li J T, Yin R W, Su X P, Wu H H, Li J J, Qin S Q, Sun S D, Chen J, Su Y J, Qiao L J, Guo D and Bai Y 2020 *Acta Mater.* **182** 250
[59] Vid Bobnar Z K, Rasă P and Adrijan L 1999 *Phys. Rev. B* **60** 6420
[60] Li J J, Li J T, Qin S Q, Su X P, Qiao L J, Wang Y, Lookman T and Bai Y 2019 *Phys. Rev. Appl.* **11** 044032
[61] Weyland F, Acosta M, Vögler M, Ehara Y, Rödel J and Novak N 2018 *J. Mater. Sci.* **53** 9393

[62] Weyland F, Acosta M, Koruza J, Breckner P, Rödel J and Novak N 2016 *Adv. Funct. Mater.* **26** 7326
[63] Novak N, Pirc R and Kutnjak Z 2013 *Europhys. Lett.* **102** 17003
[64] Li J J, Yin R W, Li J T, Su X P, Su Y J, Qiao L J and Bai Y 2023 *J. Adv. Ceram.* **12** 463
[65] Li J J, Wu H H, Li J T, Su X P, Yin R W, Qin S Q, Guo D, Su Y J, Qiao L J, Lookman T and Bai Y 2021 *Adv. Funct. Mater.* **31** 2101176
[66] Ponomareva I and Lisenkov S 2012 *Phys. Rev. Lett.* **108** 167604
[67] Wu H H and Cohen R E 2017 *J. Phys.: Condens. Matter* **29** 485704
[68] Li J T, Qin S Q, Bai Y, Li J J and Qiao L J 2017 *Appl. Phys. Lett.* **111** 093901
[69] Marathe M, Renggli D, Sanlialp M, Karabasov M O, Shvartsman V V, Lupascu D C, Grünebohm A and Ederer C 2017 *Phys. Rev. B* **96** 014102
[70] Zhou Y M, Li Q, Zhuo F P, Yan Q F, Zhang Y L and Chu X C 2018 *Ceram. Int.* **44** 9045
[71] Peräntie J, Hagberg J, Uusimäki A and Jantunen H 2010 *Phys. Rev. B* **82** 134119
[72] Goupil F L, Berenov A, Axelsson A K, Valant M and Alford N M 2012 *J. Appl. Phys.* **111** 124109
[73] Axelsson A K, Le Goupil F, Dunne L J, Manos G, Valant M and Alford N 2013 *Appl. Phys. Lett.* **102** 102902
[74] Wu H H and Cohen R 2017 *Phys. Rev. B* **96** 054116
[75] Li Z H, Li J T, Wu H H, Li J J, Wang S H, Qin S Q, Su Y J, Qiao L J, Guo D and Bai Y 2020 *Acta Mater.* **191** 13
[76] Li Z H, Wu H H, Li J J, Wang S H, Qin S Q, He J J, Liu C B, Su Y J, Qiao L J, Lookman T and Bai Y 2022 *Acta Mater.* **228** 117784